Title

Glioblastoma cells imitate neuronal excitability in humans

Authors

Tong, T[1,2], Ozsvar, A[2,3], Eschen, JT[1,2], Elbæk, KJ[1,2], Cortnum, SOS[1], Sindby, AKR[1], Kristensen, BW[4,5], Meier, K[1,2,6], Mikic, N[2,7], Sørensen, JCH[1,2], Ting, JT[8], Capogna, M[3], Hou, WH[3*], Korshøj, AR[1,2*]

Affiliations

[1]Department of Neurosurgery, Aarhus University Hospital, Palle Juul-Jensens Boulevard 165, 8200 Aarhus N, Denmark

[2]Department of Clinical Medicine, Aarhus University, Palle Juul-Jensens Boulevard 99, 8200 Aarhus N, Denmark

[3]Department of Biomedicine, Aarhus University, Høegh-Guldbergs Gade 10, 8000 Aarhus C, Denmark.

[4]Department of Pathology, The Bartholin Institute, Rigshospitalet, Copenhagen University Hospital, Blegdamsvej 9, 2100 Copenhagen Ø, Denmark

[5]Department of Clinical Medicine and Biotech Research and Innovation Center (BRIC), University of Copenhagen, Ole Maaløes vej 5, 2200 Copenhagen N, Denmark

[6]Department of Anesthesiology, Aarhus University Hospital, Palle Juul-Jensens Boulevard 165J, 8200 Aarhus N, Denmark

[7]Department of Neurosurgery, Aalborg University Hospital, Syd, Hobrovej 18-22, 9000 Aalborg, Denmark

[8]Allen Institute for Brain Science, 615 Westlake Ave N, Seattle, WA, 98109, USA.

*Corresponding authors:

Anders Rosendal Korshøj, Aarhus University Hospital, Department of Neurosurgery, Palle Juul-Jensens Boulevard J165, 8200, Aarhus N, Denmark. Email: andekors@rm.dk. Telephone: +45 78454400

Wen-Hsien Hou, Aarhus University, Department of Biomedicine, Høegh-Guldbergs Gade 10, 8000 Aarhus C, Denmark. Email: wen-hsien.hou@biomed.au.dk. Telephone: +45 52784084.

Summary

Glioblastomas (GBM) are renowned for their pronounced intratumoral heterogeneity, characterized by a diverse array of plastic cell types, which poses a significant challenge to effective targeting and treatment [1]. Recent research has documented the presence of neuronal-progenitor-like transcriptomic cell states of GBM [2, 3], notably in the leading edge of the tumor, where synaptic input from adjacent neurons drives disease proliferation [4]. However, conflicting observations regarding GBM cell excitability, ranging from non-excitable [5] to neuron-like excitability [6], add complexity to our comprehension of the pathophysiological diversity of GBM cells. Here we established a novel experimental workflow enabling comprehensive and selective investigation of the electrophysiological characteristics of cancer cells and neurons within cancer-infiltrated organotypic tissue specimens from GBM patients, using viral genetic labelling to target cellular subtypes. We observed that GBM cells exhibit distinct electrophysiological features in humans, characterized by hyperexcitability and neuron-like action potential generation. Our research provides direct evidence of excitability and a comprehensive description of the electrophysiological characteristics of GBM cells in the cancer-infiltrated cortex of humans, contributing to a deeper understanding of the cellular biology of GBM. These insights have broader implications for understanding cell-cell interactions in malignant tumors and could inform targeted therapies across diverse cancer types, offering a new lens for tackling tumor heterogeneity.

Main

Glioblastoma (GBM) is known as a highly aggressive and incurable primary brain cancer [7]. These tumors display significant resistance to comprehensive treatment including radiotherapy, chemotherapy, and surgical removal, leaving GBM patients facing a dismal prognosis.[8-10] GBMs are notably diverse in their cellular markup [1-3, 11]. In the dense tumor core, astrocytic (AS-like) and mesenchymal (MES-like) cell states form a resilient, self-repairing network, interconnected by multiple tumor microtubes (TMs) [4, 12-14] and Connexin 43 gap junctions [12, 14, 15]. In contrast, unconnected neural progenitor (NPC-like) states, resembling immature neurons in their migration dynamics, are prevalent at the tumor's infiltrative edge, moving outward from the core to colonize the surrounding brain [4]. These edge cells receive synaptic input from surrounding neurons onto one or two neurite-like TMs stimulating invasion and growth [4, 12-14, 16, 17].

Despite these intriguing features, the electrophysiological properties of GBM cells remain elusive. Specifically, it is unclear if GBM cells at the tumor edge have excitable membranes potentially enabling active integration into the surrounding tumor network and adjacent brain tissue. Preliminary analyses based on animal models and GBM cell lines have indicated a non-excitable nature of GBM cells [5, 18, 19], akin to astrocytes [20]. Conversely, one study on acute human GBM-infiltrated brain slices reported action potentials (APs) in presumed tumor cells with abnormal bipolar and multipolar morphology expressing typical glial markers, such as glial fibrillary acidic protein (GFAP) [21]. By similar notion, a few studies in animal models have reported that some low-grade oligodendroglioma and astrocytoma cells generate aberrant APs [6, 21-23]. Recently, one of these finding was further supported by the identification of a hyperexcitable neuron-like tumor cell entity at the leading edge of IDH-mutated low-grade gliomas in a PDX model, firing single aberrant APs, although these findings could not be reproduced in IDH-wildtype GBM [23].

These contradictory observations highlight the need to elucidate the intrinsic excitability of GBM cells and their physiological role in the interactions with the surrounding brain microenvironment. One of the challenges is to tackle the difficulty of identifying cellular subtypes within the leading edge of the GBM-infiltrated brain regions, as these can be elusive under acute conditions. In addition, the current understanding of the physiological attributes of GBM cells derives mainly from animal models and cell lines, limiting generalizability to humans and highlighting the need for human-based model systems.

To overcome this, we utilized a cutting-edge approach based on stable human organotypic slice cultures in combination with viral transduction tools to label and investigate cells of astrocytic and neuronal lineage selectively. This approach enabled us to identify and characterize the electrophysiological and morphological properties of both GBM cells and neurons in the cancer-infiltrated leading edge of living organotypic human samples to further corroborate their functional importance.

Results

We investigated cancer-infiltrated samples of neocortical brain tissue obtained from GBM patients during fluorescence-guided neurosurgical resection (Extended Data Fig. 1). The

samples were processed with standardized protocols [24-26], rapidly transported to the laboratory, and cut into 300-µm slices (Fig. 1a). Eligible slices contained areas with structurally preserved six-layered neocortex as well as regions of dense tumor infiltration (Fig. 1b). Using whole-cell patch-clamp recording, we immediately investigated the basic electrophysiological properties of GBM cells at the leading tumor edge and neurons residing in neocortex with no visible tumor infiltration (Fig. 1b). The leading tumor edge was defined as the area less infiltrated by the tumor, located immediately superficial to the dense tumor core and deep to the preserved neocortex (Fig. 1b). Neurons were identified directly under bright field microscopy at 40X amplification based on morphology and preserved six-layer neocortical structure, while GBM cells were identified based on morphology and tumor infiltration density. To expand our sampling capability, and to facilitate accurate preferential cell targeting, we adopted an *ex vivo* slice culture paradigm [24-26] to selectively label putative GBM cells expressing GFAP and cells of presumed neuronal lineage expressing human Synapsin-1 (hSyn1) [27], using eGFP-tagged enhancer-based Adeno-associated virus (AAV). GFAP is extensively expressed in GBM cells and not in neurons, while hSyn1 is a marker of neuronal identity [27]. We then recorded from GFAP- and hSyn1-labelled cells with soma location in the leading tumor edge and hSyn1-labelled cells in the structurally preserved cortex (Fig. 1b, middle). Cultures were preserved for recording for up to 14 days (Fig. 1a, right).

The electrophysiological properties were examined by a standardized protocol testing active- and passive membrane properties [28] (Fig.1c). Last, we confirmed the morphological and molecular identity of the recorded cells in the leading edge by using *post hoc* immunohistochemistry and 3D morphology morphological reconstruction (Fig. 1d).

Infiltrating GBM cells display aberrant action potentials

In acute brain slices, neurons located outside the GBM-infiltrated area displayed typical evoked APs, serving as a baseline for the electrophysiological behavior of GBM cells (Fig. 2a). Intriguingly, using whole-cell patch clamp recordings on acute GBM-infiltrated neocortical slices, we found that morphologically defined GBM cells at the leading tumor edge exhibited aberrant action potentials (aAPs) when depolarizing the membrane with a positive current injection (Fig. 2b; Extended Data Fig 2a, b). The identity of the patched and Alexa594/biocytin labeled GBM cells was validated based on morphology and immunostaining with colocalization with Olig2, which is commonly expressed in GBM cells at the leading tumor edge [29]. This marker was extensively expressed in all studied cases based on bulk NGS diagnostics from biopsies obtained at neighboring sites in the tumor. Olig2^{+} cells were

differentiated from oligodendrocytes based on morphology and tumor-infiltration density (Extended Data Fig. 2b, c, Extended Data Table 1).

To better characterize the active membrane properties of GBM cells and neurons, we applied AAVs to the slice cultures (Extended Data Fig. 3). This allowed for selective fluorescence labeling, identification, and targeted whole-cell patch clamping of hGFAP-expressing putative GBM cells (AAV5-hGFAP-hHEbl/E-EGFP-bGHp(A)) and hSyn1-expressing neurons (AAV1-hSyn1-EGFP-WPRE-hGHp(A)) (Extended Data Fig. 2c, Extended Data Table 1). Based on their soma location, the labeled cells were classified into three categories: 1) hSyn1-eGFP$^+$ cells residing outside the GBM-infiltrated area in structurally preserved neocortex, named hSyn1$^+$ OUT (Fig. 2c), 2) hsyn1-eGFP$^+$ cells within the GBM-infiltrated leading tumor edge, named hSyn1$^+$ IN (Fig. 2f), and 3) GFAP-eGFP$^+$ cells (Fig. 2i) within the leading tumor edge, named GFAP$^+$ IN cells, were considered to be GBM cells given the extensive tumor infiltration and abnormal cellular morphology. APs and aAPs were further defined and categorized through the normality test of the electrophysiological parameters, followed by a hierarchical cluster analysis (Fig. 3, Extended Data Fig. 4). We observed that 84.4% of hSyn1$^+$ OUT cells residing outside the GBM-infiltrated area generated normal APs (Fig. 2c-e) [24, 26]. By contrast, only 6.9% of hSyn1$^+$ IN generated APs, while 55.2% exhibited aAP properties characterized by reduced amplitude and larger half-width (Fig.2f-h). Intriguingly, 56% of hGFAP$^+$ IN cells exhibited active membrane properties upon depolarization, similar to the aAPs observed in GBM cells in the acute slices (Fig. 2i-k). The GBM identity of the patched and Alexa594/biocytin labeled GFAP$^+$ IN cells was further supported by the abnormal morphology (Extended Data Fig. The GBM identity of the patched and Alexa594/biocytin labeled GFAP$^+$ IN cells was further supported by the abnormal morphology (Extended Data Fig. 2b-c), akin to recently identified neuron-like tumor cells in low-grade glioma [23], and by their colocalization with the GBM marker Olig2 (Extended Data Fig 2b-c). We also reconstructed the virally labelled hSyn1+ IN cells which tend to have elongated processes and less primary branching from soma compared to GFAP$^+$ IN cells (Extended Data Fig. 5). Collectively, these results revealed neuron-like excitability of GBM cells and the abnormal morphology at the leading tumor edge in the GBM-infiltrated cortex.

We further evaluated the constancy of active membrane properties over culture time for hsyn$^+$ OUT, hsyn1$^+$ IN, and GFAP$^+$ IN (Extended Data Fig. 6). hSyn$^+$ OUT and hsyn1$^+$ IN cells showed weak or no correlation in each parameter, while GFAP$^+$ IN cells exhibited moderate

165 correlations, indicating dynamic changes in their voltage-dependent channels, possibly due to
166 rapid GBM cell proliferation during culture.
167

168 **GBM aAPs differ from neuronal APs**

169 We further analyzed the properties of the observed APs and aAPs by detecting both AP and
170 aAP with an initiation threshold of 20 mV/ms (Fig. 3a). We assessed the active membrane
171 properties such as amplitude, half-width, and rise/decay slopes through a long-pulse
172 depolarization step (Fig. 3c). APs and aAPs were further quantitatively defined and categorized
173 through the normality test of the electrophysiological parameters, followed by a hierarchical
174 cluster analysis (Extended Data Fig. 4). We found that $GFAP^+$ IN cells required a more
175 depolarized threshold to initiate an aAP compared to $hSyn1^+$ OUT cells and $hSyn1^+$ IN cells
176 (Fig. 3d). The aAP generated by $GFAP^+$ IN and $hSyn1^+$ IN cells had lower amplitude, wider
177 half-width, and slower rise and decay slopes compared to $hSyn1^+$ OUT (Fig. 3e-h), while there
178 was no significant difference between $GFAP^+$ IN and $hSyn1^+$ IN cells. Our results thus
179 indicated that the GBM cells displayed physiological features comparable to hSyn1+ IN cells
180 in this area.
181

182 **Na_V and K_V channels in GBM aAPs**

183 To test if the ion channels required for GFAP+ IN aAP generation were similar to those of
184 neurons, we first applied tetraethylammonium (TEA, 30 mM) to block voltage-gated potassium
185 channels in general. This caused the amplitude of the aAP to decrease notably compared to the
186 baseline (Fig. 4a-c). Additionally, we observed an increase in aAP half-width (Fig. 4d) along
187 with slower rise and decay slopes (Fig. 4e, f). Subsequent application of tetrodotoxin (TTX, 1
188 μM), a voltage-gated sodium channel blocker, eliminated the aAP (Fig. 5g). These findings
189 elucidate the cellular components involved in GFAP+ IN aAPs and further confirm that the
190 electrical excitability of GBM cells imitates that of neurons.
191

192 **Passive membrane properties differ between $GFAP^+$ IN and $hSyn1^+$ OUT/IN cells**

193 The resting membrane potential (RMP) of $GFAP^+$ IN and $hSyn1^+$ IN cells in the infiltrated
194 areas was significantly depolarized compared to that of $hSyn1^+$ OUT cells (Fig. 5a). In addition,
195 $GFAP^+$ IN and $hSyn1^+$ IN cells exhibited higher input resistance (Fig. 5b) compared to hSyn1+
196 OUT cells (Fig. 5b). The RMP and R_{in} of all groups had no significant correlation with days *in*
197 *vitro*, indicating stable passive membrane properties over the culture period. (Extended Data

198 Fig. 6). These unique characteristics of GFAP$^+$ IN cells, relatively depolarized RMP and high
199 R_{in}, mimic those of NLTs in low-grade gliomas and set them apart from astrocytes, which
200 typically have a hyperpolarized membrane, lower membrane resistance, and are unable to
201 generate aAP/APs [20], further supporting the pathological identity of these cells. hSyn1$^+$ IN
202 cells exhibited a relatively depolarized resting membrane potential, higher input resistance
203 compared to hSyn1$^+$ OUT cells.
204

205 ## Discussion

206 GBM is an incurable brain cancer characterized by significant cellular heterogeneity and
207 complex interactions with the local neuronal micro-environment. As the electrophysiological
208 features of GBM cells remain elusive, their role in neuron-cancer interactions is not fully
209 understood. Using a human-based acute slice configuration, our study provides novel and
210 robust evidence of neuron-like electrophysiological features of GBM cells at the leading cancer
211 invasion zone, contradicting recent findings from organoid and xenograft animal models [5, 18,
212 19]. These results align with recent findings of neuronal transcriptomic signatures in GBM
213 cells in this region [4, 23, 29], including NPC-like cell states [4]. In support of our findings, a
214 recent study has documented the presence of a neuron-like tumor cellular subtype in a
215 xenograft model of IDH-mutated glioma, using morphology, electrophysiology, and patch-seq
216 investigation [23]. Although similar findings could not be documented for GBM in the same
217 study, the electrophysiological and morphological features of the neuron-like low-grade tumor
218 cells were highly similar to our observations, and exhibited high input resistance,
219 hyperexcitability, glia-like morphology, and fired single aberrant APs of similar configuration.
220 The authors further observed that these neuron-like cells had co-occuring transcriptomic
221 annotations of tumor states and neurons at different levels of differentiation, raising the
222 question whether neoplastic features are induced in healthy cell states during tumor invasion,
223 or alternatively that tumor cell states potentially acquire neuronal features at the leading edge
224 to promote interaction with the surrounding microenvironment [23].
225

226 We further introduce a novel *in vitro* organotypic slice culture model designed to facilitate
227 long-term investigation of human cancer-infiltrated brain tissue using cutting edge viral genetic
228 labelling to target investigation of specific cellular subtypes. With this approach we found that
229 the majority of GFAP expressing GBM cells and hSyn1 expressing putative neurons at the
230 leading tumor edge, both displayed aberrant APs with several similarities [26, 30, 31]. In our

231 study, we found that 59% of GFAP$^+$/Olig2$^+$ GBM cells at the leading tumor edge were
232 electrically active, displaying hyperexcitability and aAPs, while exhibiting distinct
233 morphology compared to cortical neurons. Moreover, the aAP generation required voltage-
234 gated Na^+ and K^+ channels. These active membrane properties have not been observed in
235 previous animal studies documenting astrocyte-like passive electrical properties GBM cells
236 residing in the tumor core [23]. The presence of aAPs in the GBM cells may indicate unique
237 and specialized functions influencing the network excitability within the tumor-infiltrated
238 region, perhaps leading to different releasing machinery, invasion ability, proliferation
239 potential [32-34], and local network integration [6, 15], as proposed for neuron-like tumor cells
240 in low-grade glioma [23]. Furthermore, AP generation could be linked to the generation of
241 spontaneous high-frequency pathological discharge, such as epilepsy-like activity commonly
242 observed in GBM patients [35]. Understanding the functional consequence of aAPs in GBM
243 cells may provide a new understanding of the systemic tumor influence of nearby neurons
244 within the infiltrated areas.
245
246 Intriguingly, we found a striking similarity in electrophysiological properties between
247 GFAP$^+$/Olig2$^+$ GBM cells and hSyn$^+$/NeuN$^+$ cells located at the leading tumor edge.
248 Specifically, hSyn1$^+$/NeuN$^+$ cells and GFAP$^+$/Olig2$^+$ cells exhibited comparably depolarized
249 resting membrane potentials, higher membrane resistance, and a preference to generate aAPs,
250 relative to neurons in the preserved cortex. As hSyn and NeuN expression indicates neuronal
251 lineage, hSyn1$^+$/NeuN$^+$ cells may represent neurons with an altered and aberrant
252 electrophysiological phenotype due to GBM infiltration. The findings of hyperexcitability
253 within the GBM-infiltrated region, may possibly be influenced by factors like paracrine
254 glutamate secretion from GBM cells [34, 36], loss of GABAergic interneurons [37], glioma-
255 induced neuronal synaptic remodeling using GPC3 as a driver [38], and alterations of
256 potassium handling through the interaction between IGSF3 and Kir4.1 channels [18, 35].
257 Alternatively, hSyn1$^+$/NeuN$^+$ cells may represent an NPC-like cellular state of GBM, which is
258 commonly known to be enriched at the leading tumor edge [4, 23].
259
260 Collectively, our findings support emerging evidence of a complex electrical interplay between
261 neurons and GBM cells at the tumor invasion zone [5, 19]. It is known that neuronal activity
262 can promote the progression of glioma cells through paracrine signaling [34, 36] and direct
263 electrochemical synapses input [4, 5, 19]. Conversely, gliomas can influence neurons by
264 secreting non-synaptic glutamate [32, 33] and synaptogenic factors [38, 39], that drive aberrant

synaptogenesis and enhance hyperexcitability [37]. Our findings provide evidence for one missing link in this loop by which GBM cells are capable of playing an active role in the complex electrical network of the cancer-infiltrated brain. Further exploration using a diverse array of targeted viral tools is needed to unravel the role and importance of specific cell-types in this network, including GABAergic and glutamatergic subtypes, both in the tumor core and invasion zone. To this end multi-modal investigations including cellular electrophysiology and morphology in combination with single-cell, patch-seq, and spatial omics, may provide important and detailed insights towards a comprehensive cellular taxonomy of GBM. Specifically, signature morpho-electric properties of individual cell-types, akin to the recent Brain Cell Census Initiative for healthy cell-type, may reveal crucial mechanisms involved in GBM growth, invasion, resilience, and malignant self-repair, with the prospect of developing targeted therapies.

References

1. Eisenbarth, D. and Y.A. Wang, *Glioblastoma heterogeneity at single cell resolution.* Oncogene, 2023. **42**(27): p. 2155-2165.
2. Wang, Q., et al., *Tumor Evolution of Glioma-Intrinsic Gene Expression Subtypes Associates with Immunological Changes in the Microenvironment.* Cancer Cell, 2017. **32**(1): p. 42-56.e6.
3. Neftel, C., et al., *An Integrative Model of Cellular States, Plasticity, and Genetics for Glioblastoma.* Cell, 2019. **178**(4): p. 835-849.e21.
4. Venkataramani, V., et al., *Glioblastoma hijacks neuronal mechanisms for brain invasion.* Cell, 2022. **185**(16): p. 2899-2917.e31.
5. Venkataramani, V., et al., *Glutamatergic synaptic input to glioma cells drives brain tumour progression.* Nature, 2019. **573**(7775): p. 532-538.
6. Labrakakis, C., et al., *Action potential-generating cells in human glioblastomas.* J Neuropathol Exp Neurol, 1997. **56**(3): p. 243-54.
7. Louis, D.N., et al., *The 2021 WHO Classification of Tumors of the Central Nervous System: a summary.* Neuro Oncol, 2021. **23**(8): p. 1231-1251.
8. Wen, P.Y., et al., *Glioblastoma in adults: a Society for Neuro-Oncology (SNO) and European Society of Neuro-Oncology (EANO) consensus review on current management and future directions.* Neuro Oncol, 2020. **22**(8): p. 1073-1113.
9. Wick, W., et al., *Treatment of glioblastoma in adults.* Therapeutic Advances in Neurological Disorders, 2018. **11**: p. 1756286418790452.
10. Ostrom, Q.T., et al., *CBTRUS Statistical Report: Primary Brain and Other Central Nervous System Tumors Diagnosed in the United States in 2015–2019.* Neuro-Oncology, 2022. **24**(Supplement_5): p. v1-v95.
11. Verhaak, R.G., et al., *Integrated genomic analysis identifies clinically relevant subtypes of glioblastoma characterized by abnormalities in PDGFRA, IDH1, EGFR, and NF1.* Cancer Cell, 2010. **17**(1): p. 98-110.

12. Winkler, F., et al., *Cancer neuroscience: State of the field, emerging directions.* Cell, 2023. **186**(8): p. 1689-1707.
13. Osswald, M., et al., *Brain tumour cells interconnect to a functional and resistant network.* Nature, 2015. **528**(7580): p. 93-98.
14. Heuer, S. and F. Winkler, *Glioblastoma revisited: from neuronal-like invasion to pacemaking.* Trends Cancer, 2023. **9**(11): p. 887-896.
15. Hausmann, D., et al., *Autonomous rhythmic activity in glioma networks drives brain tumour growth.* Nature, 2023. **613**(7942): p. 179-186.
16. Jung, E., et al., *Tweety-Homolog 1 Drives Brain Colonization of Gliomas.* The Journal of Neuroscience, 2017. **37**(29): p. 6837-6850.
17. Gritsenko, P.G., et al., *p120-catenin-dependent collective brain infiltration by glioma cell networks.* Nature Cell Biology, 2020. **22**(1): p. 97-107.
18. Madadi, A., et al., *Correlation between Kir4.1 expression and barium-sensitive currents in rat and human glioma cell lines.* Neuroscience Letters, 2021. **741**: p. 135481.
19. Venkatesh, H.S., et al., *Electrical and synaptic integration of glioma into neural circuits.* Nature, 2019. **573**(7775): p. 539-545.
20. McNeill, J., et al., *Ion Channels and Electrophysiological Properties of Astrocytes: Implications for Emergent Stimulation Technologies.* Frontiers in Cellular Neuroscience, 2021. **15**.
21. Bordey, A. and H. Sontheimer, *Electrophysiological properties of human astrocytic tumor cells In situ: enigma of spiking glial cells.* J Neurophysiol, 1998. **79**(5): p. 2782-93.
22. Patt, S., et al., *Neuron-like physiological properties of cells from human oligodendroglial tumors.* Neuroscience, 1996. **71**(2): p. 601-11.
23. Curry, R.N., et al., *Identification of functional immune and neuronal tumour cells in glioma.* bioRxiv, 2022: p. 2022.11.05.515316.
24. Ting, J.T., et al., *A robust ex vivo experimental platform for molecular-genetic dissection of adult human neocortical cell types and circuits.* Scientific Reports, 2018. **8**(1): p. 8407.
25. Louth, E.L., et al., *Dopaminergic Neuromodulation of Spike Timing Dependent Plasticity in Mature Adult Rodent and Human Cortical Neurons.* Frontiers in Cellular Neuroscience, 2021. **15**.
26. Lee, B.R., et al., *Signature morphoelectric properties of diverse GABAergic interneurons in the human neocortex.* Science, 2023. **382**(6667): p. eadf6484.
27. Finneran, D.J., et al., *Toward Development of Neuron Specific Transduction After Systemic Delivery of Viral Vectors.* Front Neurol, 2021. **12**: p. 685802.
28. Berg, J., et al., *Human neocortical expansion involves glutamatergic neuron diversification.* Nature, 2021. **598**(7879): p. 151-158.
29. De Silva, M.I., B.W. Stringer, and C. Bardy, *Neuronal and tumourigenic boundaries of glioblastoma plasticity.* Trends Cancer, 2023. **9**(3): p. 223-236.
30. Maroso, M., *A quest into the human brain.* Science, 2023. **382**(6667): p. 166-167.
31. Siletti, K., et al., *Transcriptomic diversity of cell types across the adult human brain.* Science, 2023. **382**(6667): p. eadd7046.
32. Campbell, S.L., S.C. Buckingham, and H. Sontheimer, *Human glioma cells induce hyperexcitability in cortical networks.* Epilepsia, 2012. **53**(8): p. 1360-70.
33. Buckingham, S.C., et al., *Glutamate release by primary brain tumors induces epileptic activity.* Nat Med, 2011. **17**(10): p. 1269-74.
34. Venkatesh, H.S., et al., *Neuronal Activity Promotes Glioma Growth through Neuroligin-3 Secretion.* Cell, 2015. **161**(4): p. 803-16.

356 35. Curry, R.N., et al., *Glioma epileptiform activity and progression are driven by IGSF3-*
357 *mediated potassium dysregulation.* Neuron, 2023.
358 36. Venkatesh, H.S., et al., *Targeting neuronal activity-regulated neuroligin-3 dependency*
359 *in high-grade glioma.* Nature, 2017. **549**(7673): p. 533-537.
360 37. Campbell, S.L., et al., *GABAergic disinhibition and impaired KCC2 cotransporter*
361 *activity underlie tumor-associated epilepsy.* Glia, 2015. **63**(1): p. 23-36.
362 38. Yu, K., et al., *PIK3CA variants selectively initiate brain hyperactivity during*
363 *gliomagenesis.* Nature, 2020. **578**(7793): p. 166-171.
364 39. Krishna, S., et al., *Glioblastoma remodelling of human neural circuits decreases*
365 *survival.* Nature, 2023.
366 40. *Declaration of Helsinki – Ethical Principles for Medical Research Involving Human*
367 *Subjects.* 2008.
368 41. Ahrens, L.C., et al., *Effect of 5-Aminolevulinic Acid and Sodium Fluorescein on the*
369 *Extent of Resection in High-Grade Gliomas and Brain Metastasis.* Cancers (Basel),
370 2022. **14**(3).
371 42. Hansen, R.W., et al., *Comparison of 5-aminolevulinic acid and sodium fluorescein for*
372 *intraoperative tumor visualization in patients with high-grade gliomas: a single-center*
373 *retrospective study.* J Neurosurg, 2019: p. 1-8.
374 43. Hou, W.H., et al., *Wiring Specificity and Synaptic Diversity in the Mouse Lateral*
375 *Central Amygdala.* J Neurosci, 2016. **36**(16): p. 4549-63.
376 44. Myatt, D.R., et al., *Neuromantic - from semi-manual to semi-automatic reconstruction*
377 *of neuron morphology.* Front Neuroinform, 2012. **6**: p. 4.

378

Figure legends

Fig.1 Workflow for utilizing patient-derived GBM-infiltrated cortical tissue. a, Schematic outline of the processing of a human GBM-infiltrated neocortical specimen using acute and cultured paradigms. **b**, Cell targeting via brightfield microscopy and an adeno-associated virus-assisted gene transduction technique to selectively express fluorescence proteins in hSyn1-eGFP$^+$ cells (neurons) or GFAP-eGFP$^+$ cells (GBM cells). Scale bar under bright field is 20µm. In the 10× magnification image, the scale bar corresponds to 100µm. In the 40× magnification image, the scale bar represents 20µm. **c**, Electrophysiological characterization using fluorescence-guided whole-cell patch clamp recordings. **d**, Immunohistochemistry co-localization of Olig2 onto a Alexa594/biocytin loaded patched GFAP-eGFP$^+$ cells indicating GBM identity.

Fig. 2 GBM cells exhibit aAPs. a, Representative whole-cell recordings of neurons in acute brain slices, exhibiting APs. **b**, Representative whole-cell recordings of GBM cells in acute brain slices, displaying aAP activity. **c**, representative bright field image of a hSyn1$^+$ OUT cell expressing virally transduced hSyn1-eGFP and loaded with Alexa594 during whole-cell patch clamp recording. Scale bar: 20µm. **d**, Representative whole-cell recordings of hSyn1$^+$ OUT cells from cultured brain slices, with the majority of hSyn1$^+$ OUT displayed characteristic APs, while a subset of hSyn1$^+$ OUT exhibits aAP. **e**, Among the 28 hSyn1$^+$ OUT cells recorded from cultured slices, 22 displayed normal AP (78.5%), 4 exhibited aAP (14.3%), and 2 neurons (7.1%) show none despite membrane depolarization. **f**, Representative bright field image depicting a hSyn1$^+$ IN expressing eGFP fluorescent protein within the GBM-infiltrated cortical area. The hSyn1$^+$ IN cell was loaded with Alexa594 during whole-cell patch clamp recording. Scale bar: 20µm. **g**, Representative hSyn1$^+$ IN recording, displaying both AP and aAP. **h**, In the hSyn1$^+$ IN group, 16/29 (55.2%) cells exhibited aAP, 2/29 (6.9%) displayed APs, and 11/29 (37.9%) showed no activation. **i**, The illustrated image is a patched- GFAP$^+$ IN cell expressing eGFP within the cancer-infiltrated cortical area. The GFAP$^+$ IN cells were loaded with Alexa594 during whole-cell patch clamp recording. Scale bar: 20µm. **j**, Illustration showing the recorded aAP observed in GFAP$^+$ IN cells. **k**, Out of the 50 recorded GFAP$^+$ IN cells, 28 exhibited aAP (56%), and 22 showed no detectable response (44%).

Fig. 3. Electrophysiological characteristics of aAP/APs in GBM cells and Neurons. a-b, depictions of an AP **(a)** and aAP **(b)** during a 3ms-depolarization. Parameters measured were threshold, amplitude, half-width, and rise/decay slopes. **c.** Five parameters were compared between neurons (n = 8 cells) and GBM cells (n = 8 cells) from acute slices. Neurons showed a more depolarized threshold potential (-33.40 ± 4.14 mV, **** $P < 0.001$), a higher amplitude (67.28 ± 9.075 mV, *** $P < 0.005$), a shorter half-width (1.55 ± 0.18 ms, * $P < 0.05$), a faster rise slope (204.5 ± 49.46 mV/ms, ** $P < 0.01$), and a faster decay slope (54.37 ± 6.43 mV/ms, **** $P < 0.001$) than the GBM cells (threshold: -4.67 ± 2.22 mV, amplitude: 16.00 ± 3.23 mV, half-width: 3.02 ± 0.46 ms, rise slope: 26.51 ± 3.83 mV/ms, decay slope: 15.66 ± 2.02 mV/ms). **d**, from a holding potential of –60 mV, GFAP$^+$ IN cells showed a significantly more depolarized threshold potential (-14.24 ± 1.31 mV, n = 28 cells) than hSyn1$^+$ OUT cells (-31.60 ± 1.21 mV, n = 26 cells **** $P < 0.001$) with no significant difference between GFAP$^+$ IN cells and hSyn1$^+$ IN cells (-18.25 ± 1.82mV, n = 18 cells). hSyn1$^+$ IN cells demanded more

421 depolarization to generate APs/aAPs compared to hSyn1$^+$ OUT cells (**** $P < 0.001$). **e**,
422 GFAP$^+$ IN cells (32.91 ± 2.67 mV) and hSyn1$^+$ IN cells (38.61 ± 5.1 mV) showed significantly
423 lower amplitudes than hSyn1$^+$ OUT cells (75.84 ± 2.77 mV) (**** $P < 0.001$) with no
424 significant difference between GFAP$^+$ IN cells and hSyn1$^+$ IN cells. **f**, GFAP$^+$ IN cells (5.21±
425 0.70 ms, *** P < 0.005) and hSyn1$^+$ IN cells (4.92 ± 1.90 ms, ** P < 0.01) exhibited a broader
426 half-width compared to hSyn1$^+$ OUT cells (1.56 ± 0.14 ms) with no significant difference
427 between GFAP$^+$ IN cells and hSyn1$^+$ IN cells. **g**, GFAP$^+$ IN cells (46.24 ± 5.72 mV/ms, ****
428 $P < 0.001$) and hSyn1$^+$ IN cells (82.81 ± 20.17 mV/ms, **** $P < 0.001$) exhibited slower rise
429 slopes than hSyn1$^+$ OUT cells (247.3 ± 24.88 mV/ms) with no significant difference between
430 GFAP$^+$ IN cells and hSyn1$^+$ IN cells. **h**, GFAP$^+$ IN cells (20.18 ± 1.38 mV/ms, **** $P < 0.001$)
431 and hSyn1$^+$ IN cells (33.83 ± 4.10 mV/ms, **** $P < 0.001$) had slower decay slopes than
432 hSyn1$^+$ OUT cells (70.93 ± 5.45 mV/ms), without no significant difference between GFAP$^+$
433 IN cells and hSyn1$^+$ IN cells. **i,** Hierarchical cluster analysis of all recorded excitable cells with
434 electrophysiological parameters for classification in Extended Data Fig 4. The x-axis of the
435 dendrogram represents the individual cells. Distinct cell types are marked below the
436 dendrogram.

437 **Fig. 4. Contribution of Na$_V$ and K$_V$ Channels in aAP Generation. a**, Illustrative aAPs
438 induced by a 1-second square pulse depolarization of GFAP+ IN cells. **b**, Illustrations
439 presenting changes in aAP morphology upon application of the K$_V$ blocker TEA, highlighting
440 alterations in comparison to the control condition. **c**, comparison of amplitude parameter for
441 14 GFAP IN cells under three conditions: Control (35.13 ± 3.53 mV), TEA (25.32 ± 3.34 mV),
442 and TEA+TTX (0 mV), exhibiting a reduction in aAP amplitude in the presence of TEA ($P <$
443 0.05) and a complete absence in the combined presence of TEA and TTX ($P < 0.001$). TTX is
444 a Na$_V$ channel blocker. **d**, comparison of half-width parameter under three conditions: Control
445 (3.39 ± 0.43 ms), TEA (11.93 ± 2.64 ms), and TEA+TTX (0 ms), exhibiting a significant wider
446 in the presence of TEA ($P < 0.05$) and a complete absence in the combined presence of TEA
447 and TTX (P < 0.001). **e**, comparison of rise slope parameter under three conditions: Control
448 (46.97 ± 7.44 mV/ms), TEA (26.80 ± 4.70 mV/ms), and TEA+TTX (0 mV/ms), exhibiting a
449 significant reduction in the presence of TEA ($P < 0.01$) and a complete absence in the combined
450 presence of TEA and TTX ($P < 0.001$). **f**, comparison of decay slope parameter under three
451 conditions: Control (20.77 ± 2.14 mV/ms), TEA (13.34 ± 0.94 mV/ms), and TEA+TTX (0
452 mV/ms), exhibiting a significant reduction in the presence of TEA ($P < 0.01$) and a complete
453 absence in the combined presence of TEA and TTX ($P < 0.001$). Comparative analysis among
454 paired data from three groups was performed using a Two-way ANOVA followed by Tukey's
455 multiple comparison test. **g**, Absence of aAP induction upon depolarization after the combined
456 application of both TEA and TTX.

457 **Fig. 5. GBM cells exhibit different intrinsic membrane properties compared to neurons**.
458 **a**, hSyn1$^+$ OUT cells displayed a resting membrane potential (RMP) of -57.68 ± 1.76 mV (n =
459 31 cells) compared to -31.95 ± 2.18 mV (n = 55 cells) in GFAP$^+$ IN cells and -37.66 ± 4.32
460 mV (n = 25 cells) in hSyn1$^+$ IN cells, thus GFAP$^+$ IN cells and hSyn1$^+$ IN were more
461 depolarized compared to hSyn1$^+$ OUT cells (One-way ANOVA, Tukey's multiple comparison
462 test, **** $P < 0.001$). No significant difference was observed between hSyn1$^+$ IN and GFAP$^+$
463 IN cells. **b**, hSyn1$^+$ IN (1.53 ± 0.25 GΩ, n = 28 cells) and GFAP$^+$ IN cells (1.27 ± 0.19 GΩ, n

464 = 62 cells) displayed a significantly higher input resistance (R_{in}) compared to hSyn1$^+$ OUT
465 (0.51 ± 0.13 GΩ, n = 33 cells) (One-way ANOVA, Tukey's multiple comparison test, ** $P <$
466 0.01, * $P < 0.05$).
467

468 # Methods

469 **Glioblastoma tissue acquisition**

470 All procedures with human tissue and data were approved by and conducted in accordance
471 with the Scientific Ethics Committee for the Region of Midtjylland Denmark (official name in
472 Danish: De Videnskabsetiske Komitéer for Region Midtjylland) (journal number: 1-10-72-82-
473 17) and conducted in accordance with the ethical principles of the World Medical Association
474 Declaration of Helsinki [40]. Surgical specimens were collected at the neurosurgical
475 department at Aarhus University Hospital (Denmark) through collaboration with local
476 surgeons. Prior to participating in the study, all patients gave informed consent for the donation
477 of tissue. The patients included in the study were undergoing surgery for GBM, and the
478 obtained specimens were surgically excised cancer-infiltrated cortical tissue that required
479 removal as part of the surgical treatment. A total of nine patients were included in the study
480 (Extended Data Table 1), and the diagnoses were confirmed based on pathology examination
481 and standardized WHO criteria [7].
482 Preoperatively, the patients were administered the fluorescent compounds 5-Aminolevulinic
483 acid hydrochloride (5-ALA) (20 mg/kg bodyweight orally administered) and sodium
484 fluorescein (200 mg IV) [41, 42], which allowed the neurosurgeon to visualize the tumor and
485 the areas infiltrated by the tumor. The surgical specimens, ranging between 1-2 cm^3 in volume,
486 were resected from the superficial cortical regions and mpassed the contrast-enhancing rim of
487 the tumor. The procedure did not impose any constraints on the patients or their surgical
488 treatment. Immediately after resection, the excised specimens were placed in a sterile container
489 filled with slicing artificial cerebrospinal fluid (ACSF) as quickly as possible. The slicing
490 ACSF comprised (in mM):75 Sucrose, 84 NaCl, 2.5 KCl, 1 NaH_2PO_4, 25 $NaHCO_3$, 25 D-
491 glucose, 0.5 $CaCl_2 \cdot 2H_2O$ and 4 $MgCl_2 \cdot 6H_2O$. The pH of the solution was adjusted to 7.3–7.4
492 using concentrated hydrochloric acid, and its osmolality was confirmed to be between 295–
493 305 mOsm kg^{-1}. Before collection, the solution was pre-chilled and thoroughly bubbled with
494 carbogen (95% O_2, 5% CO_2) gas. During transportation, the tissue was continuously kept in a
495 carbogenated slicing ACSF and maintained at a constant temperature. The duration of tissue
496 transport from the operating room to the laboratory site ranged from 15 to 30 minutes.
497

498 **Tissue processing**

499 The human *ex vivo* brain slice culture method was developed based on previously established
500 procedures [24-26]. The surgical specimens were carefully examined to determine the optimal
501 approach for blocking and mounting them onto the vibrating microtome platform. To preserve
502 the integrity of dendrites and axons in the GBM-infiltrated region, the slicing angle was
503 maintained perpendicular to the pial surface. Human GBM-infiltrated brain specimens were
504 cut in sterile-filtered and chilled slicing solution that was saturated with carbogen gas to
505 maintain tissue oxygenation throughout the processing steps. Slices of 300 µm thickness were
506 cut using a Leica 1200S vibratome (Leica Microsystems, Denmark) and subsequently
507 transferred to a carbogenated (95% O_2/5% CO_2) and tempered (34 °C) slicing ACSF to recover
508 for 30 min. All the brain slices were transferred to sterile-filtered, room temperature, and low-
509 Calcium ACSF of the composition (in mM): 130 NaCl, 3.5 KCl, 1 NaH_2PO_4, 24 $NaHCO_3$, 10
510 D-glucose, 1 $CaCl_2 \cdot 2H_2O$ and 3 $MgCl_2 \cdot 6H_2O$ for the remainder of the day until used for patch
511 clamp recordings. Before utilization, the low-Calcium ACSF was equilibrated with 95% O_2,
512 5% CO_2, and its pH was adjusted to 7.3–7.4 using NaOH. Osmolality was verified to be
513 between 295–305 mOsm kg^{-1}. The slices were then divided into two groups for further
514 experiments. The first group was used directly for acute whole-cell patch-clamp. The
515 remaining brain slices were cultured and infected with fast viral vectors. Slices for interface
516 culture were placed onto membrane inserts (Millipore) in 6 well plates with 800µL per well of
517 slice culture media of the composition: 8.4 g/L MEM Eagle medium, 20% heat-inactivated
518 horse serum, 30 mM HEPES, 13 mM D-glucose, 15 mM $NaHCO_3$, 1 mM ascorbic acid, 2 mM
519 $MgSO_4 \cdot 7H_2O$, 1 mM $CaCl_2.4H_2O$, 0.5 mM GlutaMAX-I and 1 mg/L insulin, 25 U/mL
520 Penicillin/Streptomycin. The slice culture medium was carefully adjusted to pH 7.2–7.3 by
521 adding 1 M Tris base and osmolality of 295–305 mOsmoles kg^{-1} by addition of pure H_2O, and
522 sterile-filtered. Culture plates were placed in a humidified 5% CO_2 incubator at 35°C, and the
523 slice culture medium was replaced every one to two days until endpoint analysis. One to three
524 hours after brain slices were plated on cell culture inserts, brain slices were transduced by direct
525 application of concentrated AAV viral particles over the slice surface for fluorescent labelling.
526

527 **AAV-viral transduction**

528 The adeno-associated virus (AAV) vectors used in this study were acquired from the University
529 of Zurich Viral Vector Facility. We used an optimized hGFAP-AAV vector virus (ssAAV5-
530 hGFAP-hHEbl/E-EGFP-bGHp(A)) to label astrocyte or glioblastoma cells with fluorescent
531 eGFP. For labeling neurons in human brain slices, we utilized hsyn-AAV vector virus

532 (ssAAV1-hSyn-EGFP-WPRE-hGHp(A)) containing the eGFP marker. The functional virus
533 titers ranged between 1–3 × 10^{13} units per mL. To transduce human slice cultures with AAV
534 amplicons, we directly applied the concentrated viral stock solutions to the slice surface using
535 a fine micropipette, at least one hour after the initial plating to allow the slice to equilibrate.
536 The virus was carefully spread over the entire slice surface, ensuring that the surface tension
537 of the viral solution was maintained without allowing it to spread onto the surrounding
538 membrane insert, to the best possible extent.
539
540 **Patch clamp recording**
541 Human GBM-infiltrated brain slices were individually transferred to the recording chamber
542 mounted on a SliceScope microscope (Scientfica, United Kingdom). The slices were perfused
543 with carbogenated recording ACSF at a temperature of 32–35 °C, which composed of 130 mM
544 NaCl, 3.5 mM KCl, 1 mM NaH_2PO_4, 24 mM $NaHCO_3$, 10 mM glucose, 1.3 mM $CaCl_2 \cdot 4H_2O$
545 and 0.9 mM $MgSO_4 \cdot 7H_2O$. A SciCam Pro camera (Scientifica, United Kingdom) was used for
546 visualization and image capture. For whole-cell recordings, borosilicate glass pipettes (Harvard
547 glass capillaries, GC120F-10) were pulled on a horizontal pipette puller (DMZ universal
548 electrode puller, Zeitz, Germany) to a resistance of 5–7 MΩ. The pipettes were filled with an
549 internal solution comprising 126 mM K-gluconate, 10 mM HEPES, 4 mM Mg-ATP, 0.3 mM
550 Na_2-GTP, 4 mM KCl and 10 mM phosphocreatine. The pH was adjusted to 7.3–7.4 with
551 concentrated KOH and the osmolality was adjusted to 290 mOsmoles/Kg using sucrose. To
552 assist with visualization of cell filling, the internal solution was supplemented with 8 mM
553 biocytin and 50 µM Alexa 594 dye. The pipette was mounted on a Multiclamp 700B amplifier
554 headstage (Molecular Devices, United States) fixed to a micromanipulator (PatchStar,
555 Scientifica). Electrophysiology signals were recorded using a Digidata 1550B low-noise data
556 acquisition system (Molecular Devices, United States). The data were low-pass filtered at 2
557 kHz and digitized at 20 kHz. The theoretical liquid junction potential was calculated at −11
558 mV but was not corrected. Once a whole-cell recording was established, pipette capacitance
559 was neutralized, and bridge balance was applied. After forming a stable seal and breaking in,
560 the resting membrane potential was recorded within the first minute. The holding potential in
561 the voltage clamp mode was set at -60 mV. For inclusion in the analysis, cells were required to
562 have a > 1 GΩ seal recorded before break-in and a series n initial access resistance < 20 MΩ.
563 After the patch-clamp experiment, the X-, Y-, and Z-positions of all patched cells, as well as
564 the margin of slices, were recorded in a coordinate file. This coordinate data was subsequently
565 utilized to discern the identity of the patched cells in the immunohistochemistry experiment.

566

567 **Electrophysiological data analysis**

568 Electrophysiological data were analyzed using Clampfit 10.7 software (Molecular Devices,
569 United States). The resting membrane potential was determined by averaging the voltage
570 values recorded for 1 minute under current clamp mode (I = 0). Input resistance (R_{in}) was
571 calculated from the linear portion of the current−voltage relationship, generated in response to
572 a series of 1-second current injections (ranging from -100 to +50 pA in 10 or 20 pA steps). The
573 maximum and steady-state voltage deflections were used to determine the maximum and
574 steady-state R_{in}, respectively.

575 For the differentiation of APs and aAPs, individual potentials were elicited by applying 3 ms
576 direct current injections with increasing amplitudes, which was selected for analysis of
577 AP/aAPkinetics. The initiation of APs/aAPs was defined as the voltage at the time
578 corresponding to when the first derivative of the voltage response first exceeded 20 mV/ms
579 [43]. Five distinct parameters were computed for each AP/aAP: Threshold potential (mV),
580 amplitude (mV), half-width, maximum rise slope (mV/ms), and maximum decay slope (mV/ms)
581 (Supplementary Fig. 3a). The amplitude of APs/aAP was measured from the threshold to the
582 peak voltage. The half-width of AP/aAP was determined as the width at half-maximal
583 amplitude. To determine the rise and decay slopes of APs/aAPs, measure the duration for which
584 the membrane potential ascends from 10% to 90% of the peak amplitude and descends from
585 90% to 10% of the peak amplitude. Subsequently, divide the amplitude by the corresponding
586 time intervals.

587 To ascertain the optimal parameter combinations that could effectively classify AP and aAP
588 signatures, a hierarchical clustering analysis was performed by using squared Euclidean
589 distances [43] . Five AP parameters were tested by the D'Agostino–Pearson normality test.
590 Parameters with a non-Gaussian distribution were used for subsequent unsupervised clustering.
591 Before clustering, we first normalized variables into the range (0, 1) by performing min–max
592 normalization. Hierarchical clustering arranges data items into a tree-like dendrogram in which
593 tree leaves represent data items, and the length, or the computed Euclidean distance, of tree
594 edges between leaves represents the dissimilarity between data items. The hierarchical
595 clustering analysis was performed with the Free Statistics Software (Office for Research
596 Development and Education, version 1.1.23-r7, http://www.wessa.net/).

597 The electrophysiological data obtained from acute and cultured brain slice experiments,
598 evaluating features over time post-slicing, were analyzed using linear regression and Pearson's
599 correlation. The sample size, p-values, and R^2 values were reported.

600 To confirm the components of aAPs, Tetraethylammonium chloride (TEA, Sigma-Aldrich,
601 30mM) was first added to the superfusing ACSF, followed by the subsequent addition of
602 tetrodotoxin citrate (TTX, TOCRIS, 1 μM) to the ACSF. The amplitude, half-width, and rise
603 and decay slopes of AP/aAP from each cell were compared between the control, TEA, and
604 TTX+TEA conditions.
605
606 **Immunocytochemistry**
607 All the virus transduced slices or patched slices were fixed in 4% paraformaldehyde in
608 phosphate buffered saline (PBS) at 4 °C overnight and then transferred to 0.1 M PBS. The fixed
609 slices were then transferred to 0.1 M PBS and washed thoroughly three times to remove any
610 remaining fixative. Next, the slices were incubated in 0.1 M PBS containing 0.5% Triton-X-
611 100 (0.5% PBST) for 30 minutes at room temperature. To block nonspecific binding sites, the
612 slices were incubated in 0.5% PBST containing 10% bovine serum albumin (BSA) (Sigma-
613 Aldrich, A4503) for 5-6 hours at room temperature. Following the blocking step, the slices
614 were incubated at 4 °C for 48 hours in 0.5% PBST containing 5% BSA and one or more primary
615 antibodies. After the 48-hour incubation with primary antibodies, the slices were washed three
616 times for 10 minutes each with 0.1 M PBS. Subsequently, they were incubated for 2 hours at
617 4 °C with the appropriate secondary antibodies. After incubation with appropriate secondary
618 antibodies, slices were washed for 10 min three times with PBS, followed by DAPI nuclear
619 staining for 15-20 min at room temperature. After washing the slices for 10 min three times
620 with PBS with. Slices were treated with 0.1% Sudan Black B (Sigma-Aldrich, Saint Louis,
621 MO) in 70% ethanol to quench lipofuscin autofluorescence. The slices were then dried on glass
622 microscope slides and mounted with anti-fade solution (Sigma-Aldrich, F4680). Slides were
623 stored at room temperature in the dark prior to imaging. Confocal z-stack images were acquired
624 on a spinning disk confocal microscope (Olympus IX83) equipped with 504 nm, 488 nm, 594
625 nm, and 647 nm excitation laser lines. Images were acquired using a ×20 objective with a
626 numerical aperture (NA) of 0.9.
627
628 **Morphology reconstruction**
629 The morphology of the cells was reconstructed from a stack of 116–196 images per cell for
630 hSyn+ IN cells using a 488 nm excitation laser for eGFP fluorescence signal. GFAP+ IN cells
631 were reconstructed from a stack of 24–43 images per cell using a 594 nm excitation laser for

632 the Alexa-594 loading dye. Image stacks belonging to one cell were imported into the
633 Neuromantic 1.7.5 software [44] for 3D reconstruction.
634
635 **Antibodies**
636 The primary antibodies: Mouse anti-NeuN (1:500 dilution, Chemicon, MAB377); Rabbit anti-
637 GFAP (1:500 dilution, Abcam, ab68428). Goat anti-Olig2 (1:500 dilution, Biotchne, AF2418).
638 The secondary antibodies: CY^{TM}5 (Donkey anti Mouse, 1:400, Jacksonimmuno, AB2340820);
639 CY^{TM}5 (Donkey anti Rabbit, 1:400 dilution, Jacksonimmuno, AB2340607); Alexa 647
640 (Donkey anti Goat, 1:400 dilution, Invitrogen, A-21447); Alexa Fluor™ 594 (Donkey anti
641 Rabbit 1:400 dilution, Invitrogen, A-21207); Alexa Fluor™ 594 (Goat anti-Mouse, 1:400,
642 Jacksonimmuno, AB2338871); Alexa Fluor™ 594 (conjugated streptavidin binding for
643 biocytin, 1:400, Thermofisher, S11227).
644
645 **Statistical Analysis**
646 Sample sizes and statistical tests are provided in the figure legends. Statistical analysis was
647 performed using GraphPad Prism 8 (GraphPad Software, United States). All data are presented
648 as mean ± SEM. When more than two groups were compared, a One-way ANOVA was used,
649 followed by Tukey's multiple comparison test. Comparative analysis among paired data from
650 three groups was performed using a Two-way ANOVA followed by Tukey's multiple
651 comparison test. To evaluate correlations for each electrophysiological parameter, using linear
652 regression and Pearson's correlation is applied to the data. R^2 and P values are calculated for
653 each fitting to indicate correlation strength and significance. The independent t-test was used
654 to assess differences among the five parameters of APs and aAPs. Data are presented as the
655 mean ± SEM. Levels of statistical significance are indicated as follows: *$p<0.05$, **$p<0.01$,
656 ***$p<0.001$, and ****$p<0.0001$.
657
658 **Acknowledgements**
659 We thank K. Widzsiz for technical assistance and L.M. Fitting for logistical and technical
660 assistance; H. Thygesen, A. Kobberø, and A.S. Møller-Andersen for administrative assistance;
661 the OR staff at the Department of Neurosurgery, Aarhus University Hospital, for logistical
662 assistance; E.M.R. Jensen for assisting patient enrolment.
663
664 **Author contributions**

A.R.K. and M.C. conceived and conceptualized the project. T.T., A.O., W-H.H., MC, and A.R.K designed the experiments. T.T., A.O, and W-H.H. conducted and analyzed the electrophysiology experiments. J.T.E. contributed to immunofluorescence and morphology experiments and manuscript editing. S.O.S.C, A.K.R.S., and A.R.K. contributed with patient inclusion and performed surgical procedures. K.M. provided data structure and management of patient data and N.M. contributed with entry of data and meta data. B.W.K. supervised immunostaining and histopathology experiments and contributed to manuscript editing. T.T., W-H.H., K.J.E., and A.R.K. wrote the manuscript draft and all authors contributed critical editing. A.R.K. contributed funding and was responsible for project administration and management. A.R.K. and W-H.H. supervised all aspects of the work.

Competing interests declarations

None.

Fig. 1

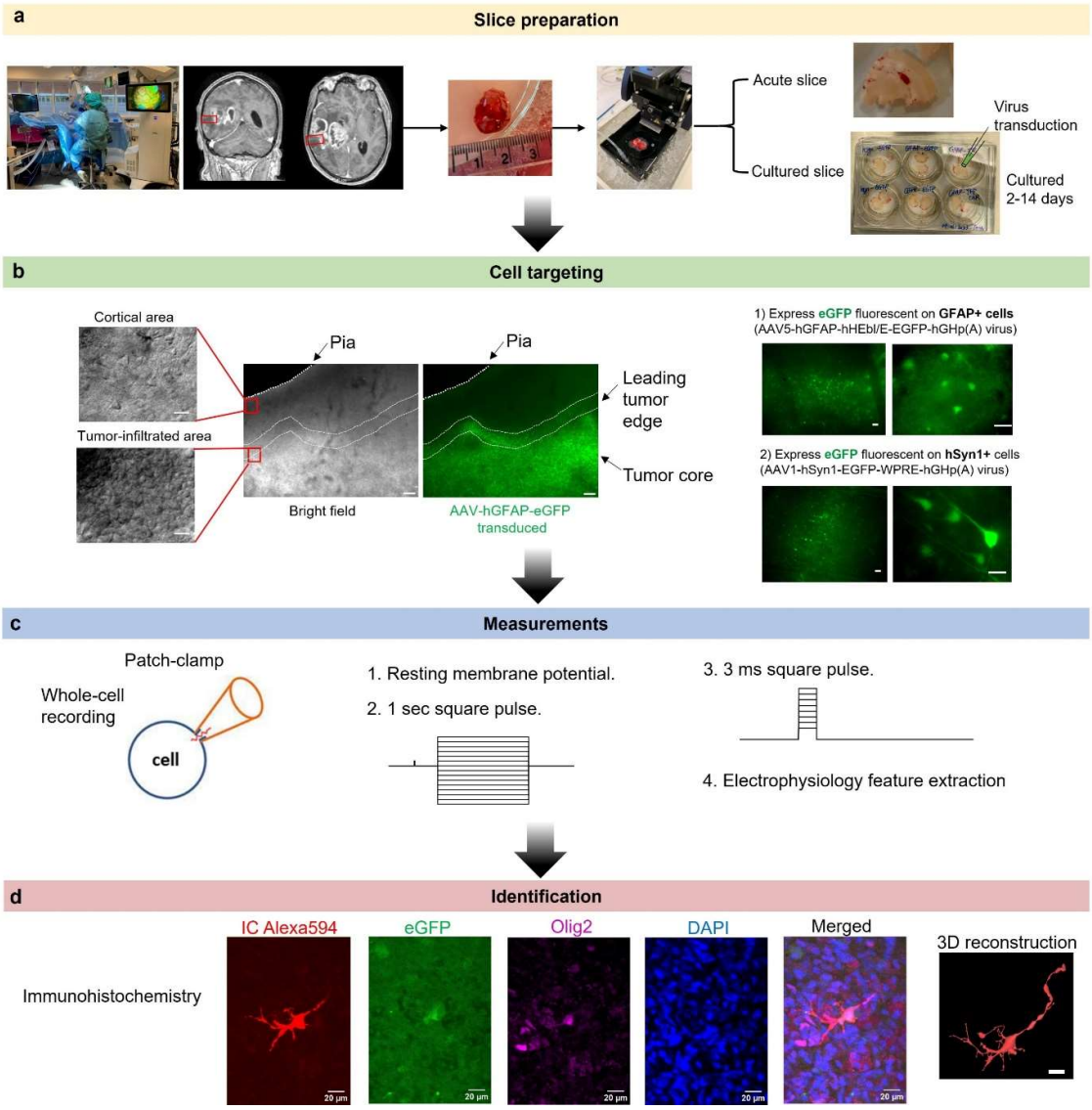

698

699

700

701

702

703

704

705

Fig. 2

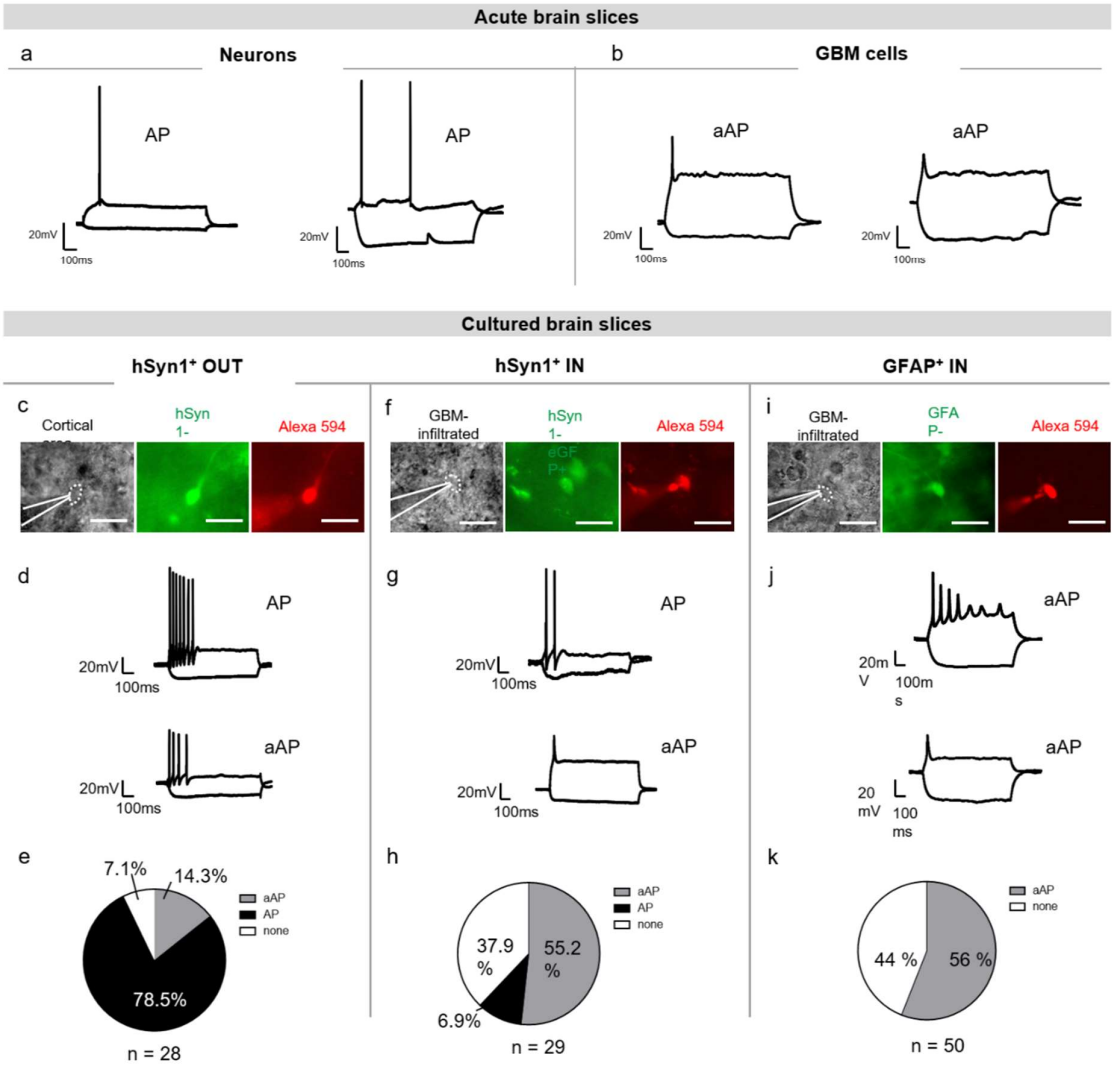

706

707

708

709

710

711

712

713

714

Fig. 3

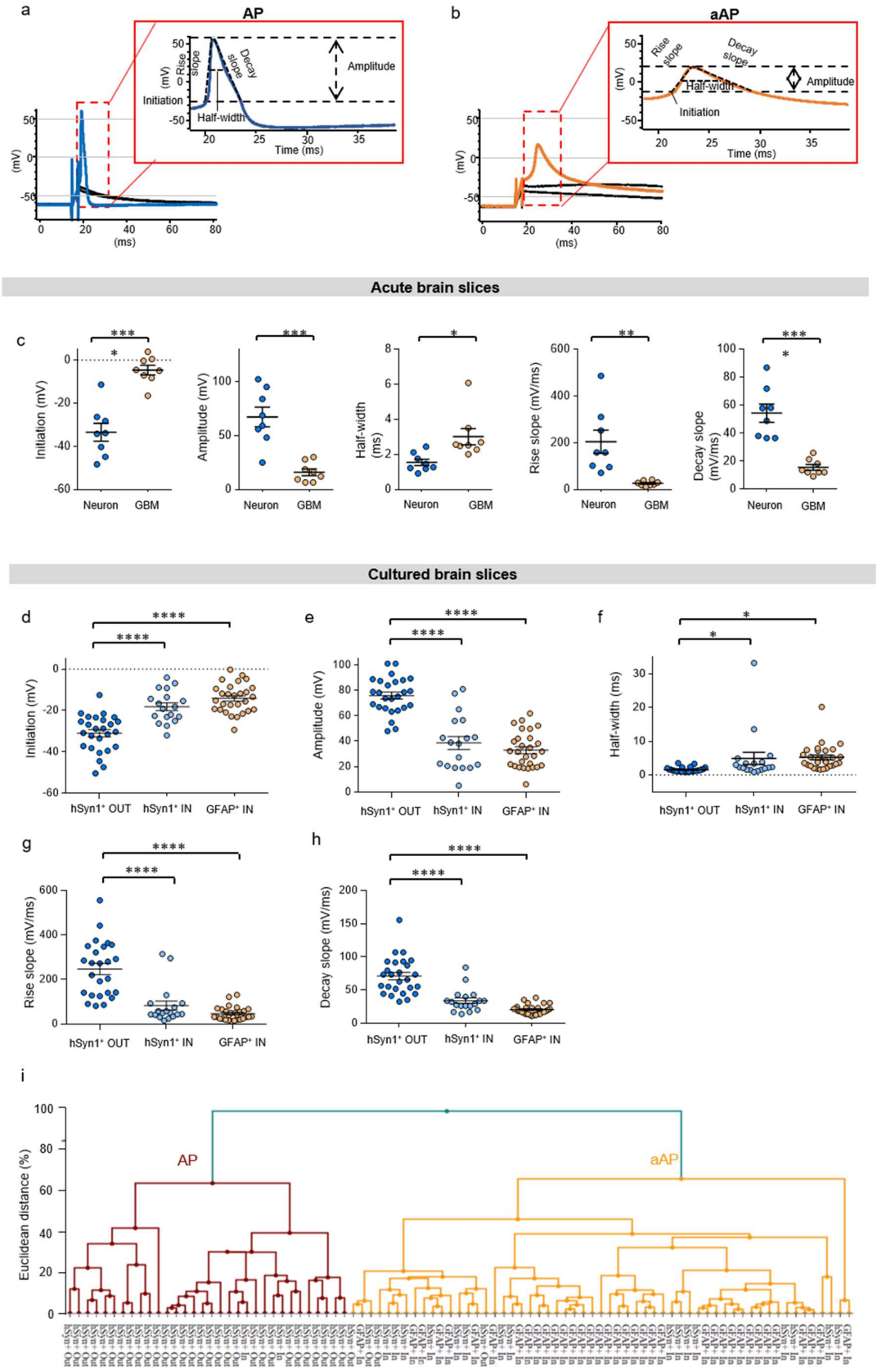
a
AP
Rise slope
Decay slope
Amplitude
Initiation
Half-width
Time (ms)
(mV)
(ms)
b
aAP
Rise slope
Decay slope
Half-width
Amplitude
Initiation
Time (ms)
Acute brain slices
c
Initiation (mV)
Amplitude (mV)
Half-width (ms)
Rise slope (mV/ms)
Decay slope (mV/ms)
Neuron
GBM
Cultured brain slices
d
e
f
g
h
Initiation (mV)
Amplitude (mV)
Half-width (ms)
Rise slope (mV/ms)
Decay slope (mV/ms)
hSyn1⁺ OUT
hSyn1⁺ IN
GFAP⁺ IN
i
Euclidean distance (%)
AP
aAP

Fig. 4

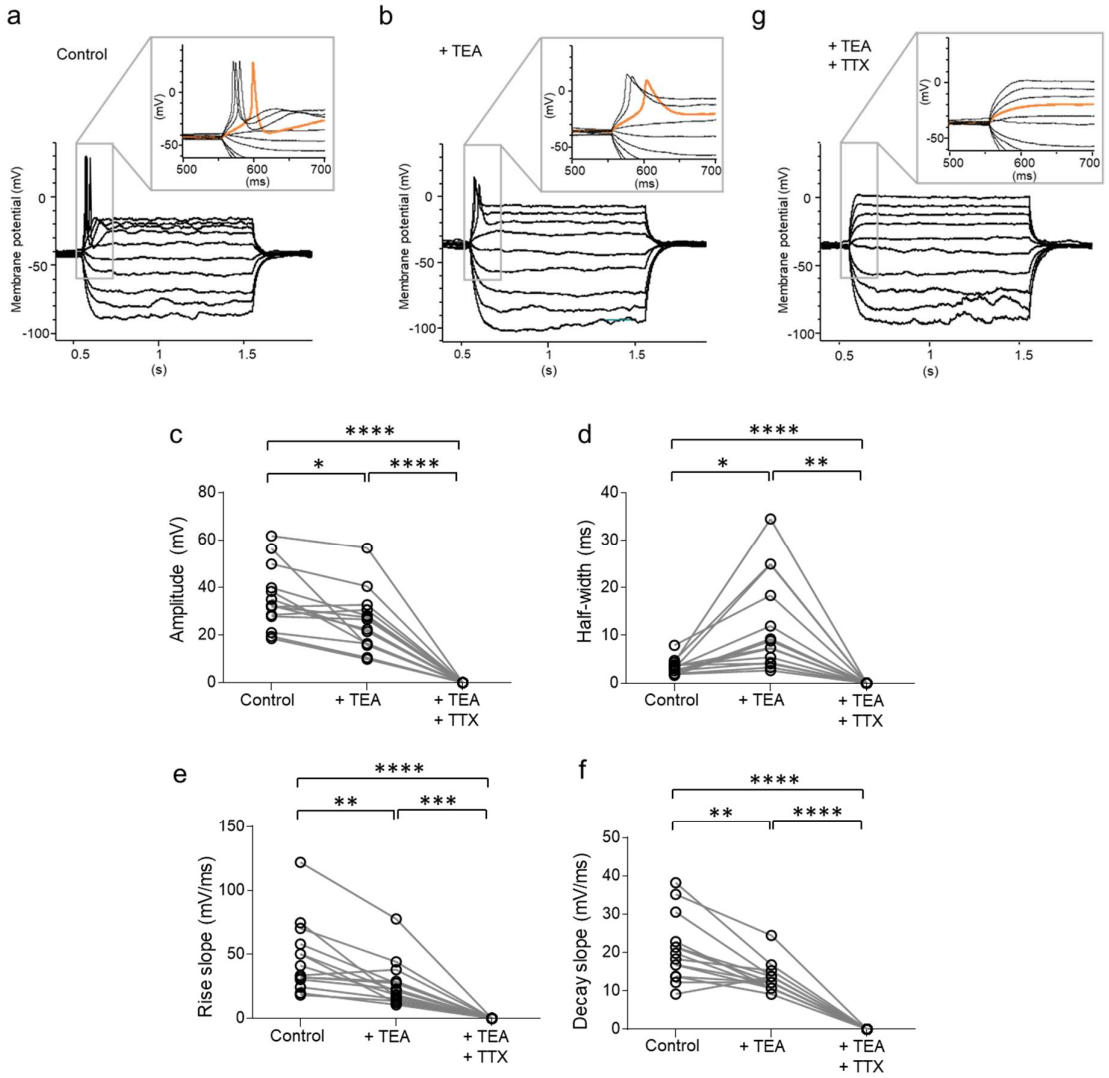

715

716

717

718

719

720

721

722

723

Fig. 5

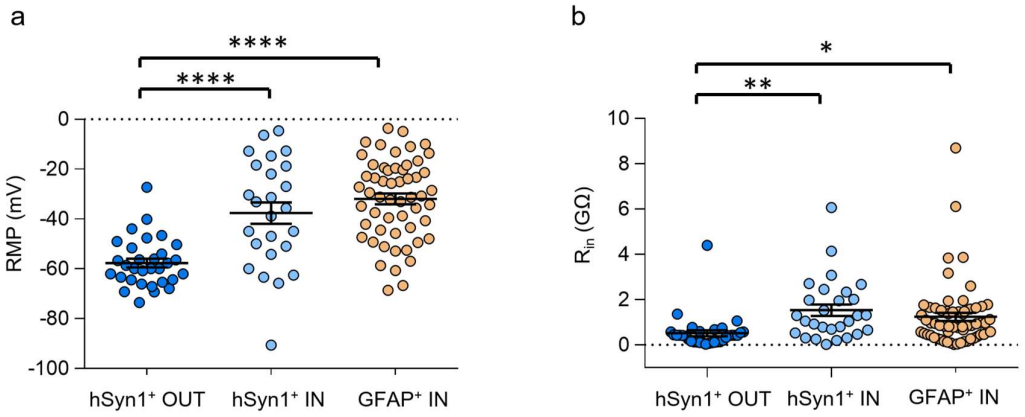
a
****
****
0
-20
-40
-60
-80
-100
RMP (mV)
hSyn1+ OUT
hSyn1+ IN
GFAP+ IN
b
*
**
10
8
6
4
2
0
Rin (GΩ)
hSyn1+ OUT
hSyn1+ IN
GFAP+ IN

724